Journal of Power Sources 413 (2019) 367–375

Contents lists available at ScienceDirect

Journal of Power Sources

journal homepage: www.elsevier.com/locate/jpowsour

Iron oxide and phosphide encapsulated within N,P-doped microporous carbon nanofibers as advanced tri-functional electrocatalyst toward oxygen reduction/evolution and hydrogen evolution reactions and zinc-air batteries

Min Wang[a], Chengtian Zhang[a], Tian Meng[a], Zonghua Pu[a], Huihui Jin[a], Daping He[a,b], Jianan Zhang[c,**], Shichun Mu[a,b,*]

[a] State Key Laboratory of Advanced Technology for Materials Synthesis and Processing, Wuhan University of Technology, Wuhan, 430070, China
[b] Hubei Engineering Research Center of RF-Microwave Technology and Application, Wuhan University of Technology, Wuhan, 430070, China
[c] College of Materials Science and Engineering, Zhengzhou University, Zhengzhou, 450001, China

HIGHLIGHTS

- A tri-functional electrocatalyst is prepared by an electrospinning method.
- FeP and Fe_3O_4 nanoparticles are embedded in N,P-doped microporous carbon nanofibers.
- It shows high performance for oxygen reduction, hydrogen/oxygen evolution reactions.
- Active species in electrocatalysts toward electrocatalytic reactions are revealed.
- The disposable zinc-air battery with the as-made catalyst shows high power density.

GRAPHICAL ABSTRACT

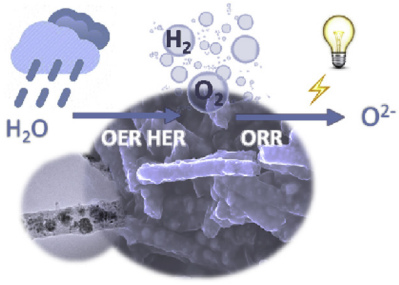

ARTICLE INFO

Keywords:
Iron compounds
Carbon nanofibers
Electrospinning
Tri-functional electrocatalysts
Zinc-air battery

ABSTRACT

Developing cheap, efficient and stable tri-functional catalysts can reduce the producing process of catalysts for different electrochemical energy conversion devices, therefore being important to their commercialization. In light of this, we firstly report an advanced catalyst with both FeP and Fe_3O_4 nanoparticles embedded in N,P-doped microporous carbon nanofibers obtained by electrospinning. The resultant catalyst exhibits robust catalytic activities towards oxygen reduction reaction, hydrogen evolution reaction and oxygen evolution reaction, all of which surpass or are comparable to previously reported tri-functional catalysts. The Fe_3O_4 nanoparticles and N-doped carbon are the main active species toward oxygen reduction reaction and oxygen evolution reaction, while FeP nanoparticles remarkably promote the hydrogen evolution reaction. The catalyst also shows excellent oxygen reduction stability due to the unique nanoparticle-embedded microporous carbon nanofibers structure. Furthermore, the obtained tri-functional catalyst is also applied in a disposable zinc-air battery, showing good performance. This work offers an effective method to construct a tri-functional catalyst in electrochemical energy devices.

* Corresponding author. State Key Laboratory of Advanced Technology for Materials Synthesis and Processing, Wuhan University of Technology, Wuhan, 430070, China.
** Corresponding author.
E-mail addresses: zjn@zzu.edu.cn (J. Zhang), msc@whut.edu.cn (S. Mu).

https://doi.org/10.1016/j.jpowsour.2018.12.056
Received 27 September 2018; Received in revised form 1 December 2018; Accepted 18 December 2018
0378-7753/

1. Introduction

To reduce the environmental pollution and the reliance on fossil fuels, many efforts have been devoted to developing eco-friendly energy conversion devices, such as water electrolyser and fuel cell. Oxygen reduction reaction (ORR) is the most important electrochemical reaction in fuel cells and metal-air batteries, while hydrogen evolution reaction (HER, $2H^+ + 2e^- \rightarrow H_2$), oxygen evolution reaction (OER, $2H_2O \longrightarrow 4e^- + 4H^+ + O_2$) are two main reactions in the water splitting process [1,2]. However, in fuel cells and zinc-air batteries ($2Zn + O_2 \rightarrow 2ZnO$) both ORR and OER are kinetically sluggish, and often need to be catalyzed by precious metals (e.g. Pt, Ir or Ru) [1,2]. Even though the precious metal-based catalysts have prominent electrochemical activity, their high cost, poor durability greatly limit the commercialization of energy conversion devices. Besides, different precious metal catalysts only work with certain reactions. For instance, Ir and Ru are only capable of catalyzing OER while Pt only work well with ORR and HER. Such selectivity adds extra processes to the fabrication of various catalysts for energy conversion devices. Therefore, a low-cost and non-selective (i.e. multi-functional) catalyst, as the substitution of precious metal-based catalysts, is needed urgently.

For such purpose, many non-noble metals-based electrocatalysts have been widely studied. Among non-noble metals, iron received exceptional attention due to abundant sources and high activities of its derived catalysts (especially Fe-N-C catalysts) towards ORR, OER or HER [3,4]. For example, iron oxides [5,6], nitrides [7] or hydroxides [8,9] combined with N-doped carbon are active to ORR or OER, while iron phosphides or iron doped transition metal phosphides usually show high HER activity [10–12]. On the other hand, encapsulating iron compounds in fibrous, tubular or spherical nanoscale carbon shells can usually lead to better ORR activity and stability [2,13]. This is because the synergistic effect between inner metal species and outer carbon shell increases the overall electrochemical activity of the catalyst. Also, the carbon shell is able to protect the inner metal species from fast corrosion by electrolyte, and therefore improve the stability of the catalyst [14,15].

Electrospinning technique is a well controllable method for generating such core-shell-like structure nanofibers. Based on this technique, it is easy to obtain the nanoparticles-embedded carbon nanofibers with different porosity and containing different metal species by adjusting the electrospinning solution and pyrolysis ways [16–18]. After heteroatom-doping, the carbon shells turn to be active and can be used to confine the iron-based nanoparticles as well as activate the iron-based electrocatalysts [13,16,19]. Up to now, several Fe-based bifunctional electrochemical catalysts toward ORR/OER [20], ORR/HER [16] or OER/HER [21] have been reported. However, the tri-functional catalysts with good ORR, HER and OER activities are still rarely reported, although they are promising for reducing the complexity and cost of electrochemical energy conversion devices.

Herein, the N,P-doped carbon nanofiber encapsulated Fe_3O_4 and FeP nanoparticles are firstly prepared and used as tri-functional catalyst toward ORR, OER and HER. The as-made catalyst exhibits prominent ORR performance over commercial Pt catalysts, excellent HER and OER catalytic activities. It is found that, Fe_3O_4 and N-doped carbon are main active species for ORR and OER, while FeP remarkably improve the HER activity in both acid and basic solutions. The obtained tri-functional catalyst is also applied in zinc-air batteries. The maximum power density of zinc-air battery with FeCNFs-NP electrode is as high as 97 mW cm^{-2}.

2. Results and discussion

2.1. Structure properties

As depicted in Fig. 1, the catalyst was prepared by a three-step method. First, the electrospinning technique was used to fabricate PAN/Fe carbon nanofibers (CNFs). Then, N-doped CNFs containing Fe_3O_4 nanoparticles (FeCNFs-N) were obtained through oxidative stabilization [22] at 240 °C followed by a carbonization process at 800 °C. FeCNFs-N was subsequently annealed in N_2 in the presence of NaH_2PO_2 at 350 °C to transform some of Fe_3O_4 into FeP nanoparticles via the phosphating reaction. Then the final product FeCNFs-NP was gained.

Fig. 2a exhibits the XRD spectra of FePAN-O, FeCNFs-N and FeCNFs-NP. For FePAN-O (black line), the broad peak displayed at around 26° can be ascribed to amorphous carbon, suggesting the absence of crystallization during the oxidative stabilization process. After carbonization, all the sharp diffraction peaks emerged in pattern of FeCNFs-N (blue line) can be ascribed to Fe_3O_4 [5]. The three new peaks for FeCNFs-NP (red line) are corresponding to (011) (121) (211) planes of FeP, indicating successful transformation of partial Fe_3O_4 to FeP during the phosphating process [11,23]. The fitting result of XRD pattern of FeCNFs-NP (Fig. S1) further shows that the peak area ratio of Fe_3O_4 to carbon is 0.5379, and FeP to carbon is 0.1145, suggesting the higher content of Fe_3O_4 in the catalyst.

To investigate the graphitization degree of FeCNFs-N and FeCNFs-NP, Raman measurements were conducted. As illustrated in Fig. 2b, the intensity of peak located at *ca.* 1360 cm^{-1} (I_D) relates to the vibrations of the sp^3 carbon atoms of defects and disorder, while the intensity of the peak located at *ca.* 1590 cm^{-1} (I_G) results from the crystallinity of sp^2 carbon materials [24]. The ratios of I_D to I_G of FeCNFs-N and FeCNFs-NP are 0.925 and 0.92, respectively, indicating the negligible effect of the P-doping process on graphitization degree of the samples. Fig. 2c displays the BET results of FeCNFs-NP and Fesol-NP. It is found that the sample synthesized through the electrospinning method (FeCNFs-NP) has the specific surface area (SSA) as high as 288.8 $m^2 g^{-1}$, which is twice larger than the sample prepared through the solvent evaporation method (Fesol-NP, SSA = 143.2 $m^2 g^{-1}$). The pore size distribution (inset of Fig. 2c) exhibits that Fesol-NP has a wide peak at 0.61 nm while FeCNFs-NP has a much stronger peak at a similar position (0.67 nm), indicating a more uniform microporous structure of FeCNFs-NP. Such uniform structure and large SSA are beneficial for reactants to approach the active sites on catalysts, therefore increasing the electrocatalytic performance of FeCNFs-NP [25]. This result suggests that the nanoparticle-embedded microporous nanofiber structure derived from the electrospinning method is of great importance.

Morphologies and structures of the catalysts were investigated via SEM and TEM techniques. As shown in Fig. 3a and b, FePAN-O consists of randomly oriented amorphous CNFs with smooth surfaces and average diameters about 150 nm. Fig. 3c and d illustrate the structure of FeCNFs-NP. It is found that after carbonization and phosphating treatments, FeCNFs-NP presents a well-defined nanoparticles-embedded nanofiber structure with Fe_3O_4 and FeP nanocrystals encapsulated in the N,P-doped carbon shell. The thickness of N,P-doped carbon shell is around 6.5 nm (inset of Fig. 3d). The clear lattice fringes with spacing of 0.2 nm and 0.21 nm in Fig. 3e correspond to the (210) planes of FeP and (400) facets of Fe_3O_4, respectively. This result is consistent with that of XRD. The EDX spectrum (Fig. 3f) in the selected area (inset of Fig. 3f) of FeCNFs-NP confirms the coexistence of Fe, O, P, N and C elements. The elemental mapping images (Fig. 3g) further reveal the uniform distribution of N, P atoms in CNFs and the nanoparticles-embedded structure. For comparison, the SEM and corresponding Fe, C mapping images of Fesol-NP, synthesized with a solution evaporation method, are also given in Fig. S2a and b, respectively. Fesol-NP presents an irregular block structure with iron species insert between carbon matrixes.

In addition to elemental mapping and EDX images, the element composition and valence states of FeCNFs-NP was also gained from XPS (Fig. 4a–d). The percentage of each element is displayed in Table S1. As shown in Fig. 4a, four elements (Fe, N, C and O) exist on the surface of sample FeCNFs-N, whereas after the phosphating treatment, a new peak for P element appears (sample FeCNFs-NP), suggesting the successful doping of P. This result is also consistent with the XRD result. For the

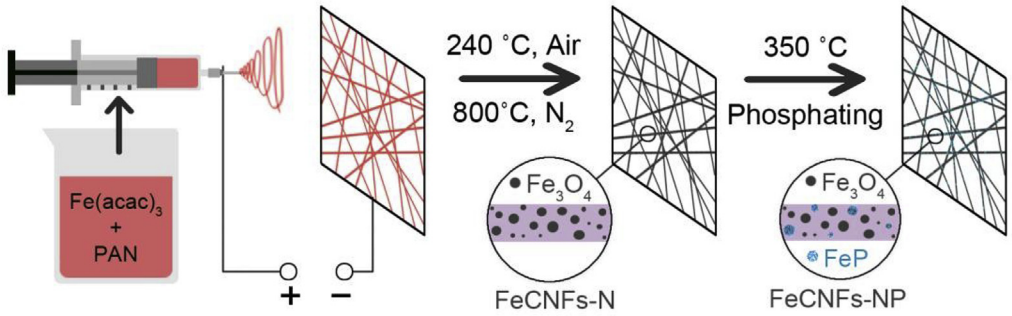

Fig. 1. Schematic illustration for preparation of FeCNFs-NP.

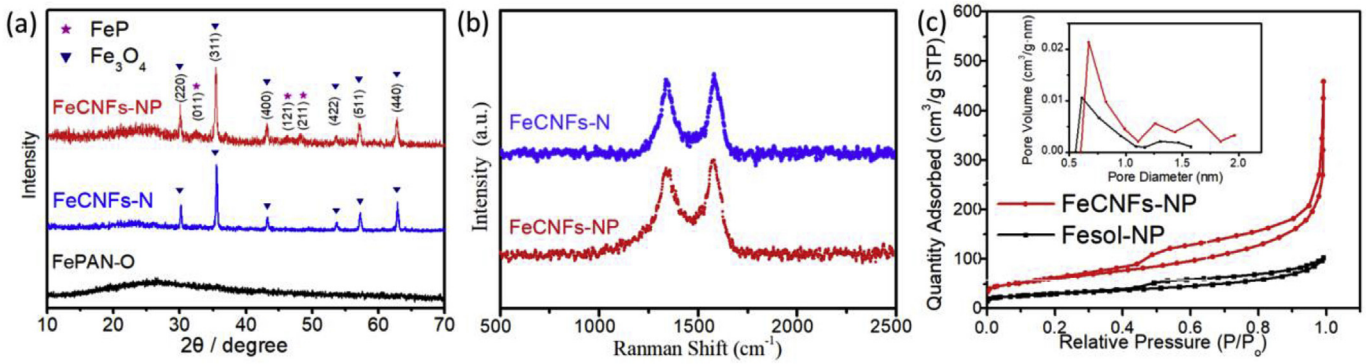

Fig. 2. (a) XRD patterns of FeCNFs-NP, FeCNFs-N and FePAN-O. (b) Raman spectra of FeCNFs-NP and FeCNFs-N. (c) N_2 adsorption/desorption isotherms of FeCNFs-NP and Fesol-NP.

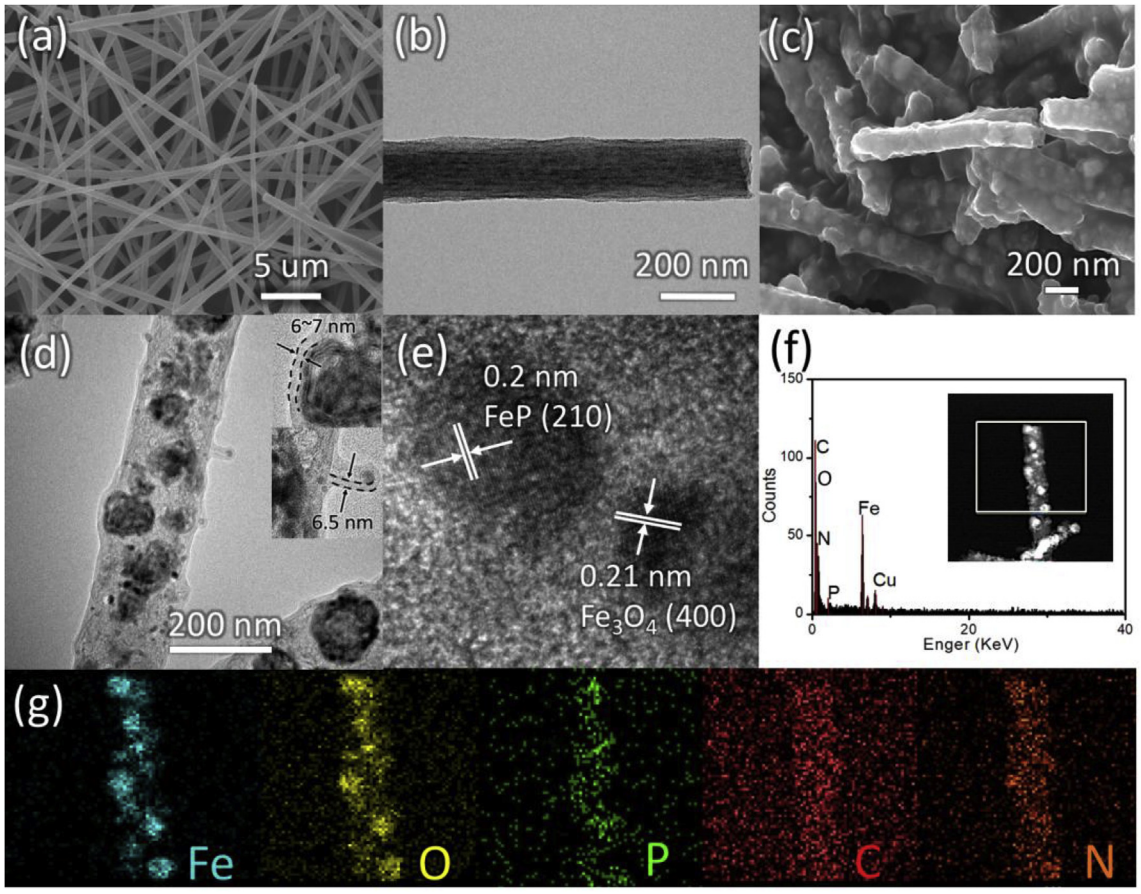

Fig. 3. (a) SEM and (b) TEM images of FePAN-O. (c) SEM, (d) TEM and (e) HRTEM images of FeCNFs-NP. (f) EDX spectrum of FeCNFs-NP (insert shows the measured area), (g) corresponding elemental mappings of FeCNFs-NP.

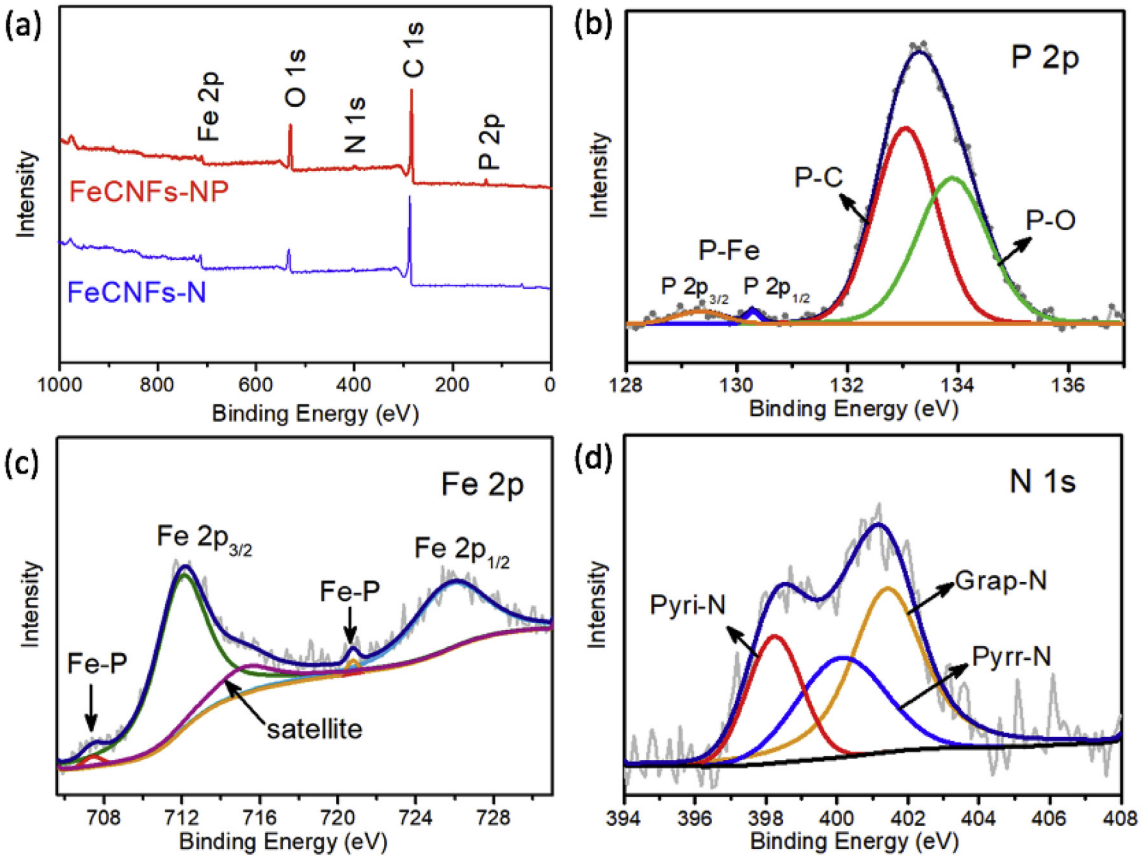

Fig. 4. (a) XPS survey spectra for FeCNFs-NP and FeCNFs-N. XPS spectra in (b) P 2p, (c) Fe 2p, (d) N 1s regions for FeCNFs-NP.

high-resolution P 2p spectrum (Fig. 4b), the peaks at 129.2 and 130.3 eV correspond to the P $2p_{3/2}$ and P $2p_{1/2}$ of Fe-P, while the peaks at 133.0 and 133.9 eV can be assigned to P-C and P-O, respectively [26]. The formation of P-O is probably due to the unavoidable surface oxidation of catalyst to air [27]. In the high-resolution Fe 2p region (Fig. 4c), the peaks at 707.4 and 720.7 eV can be ascribed to Fe 2p3/2 and Fe 2p1/2 of FeP, respectively [28,29], while the peaks at 711.9 and 725.6 eV correspond to iron oxides [6,30]. The additional peak is the satellite peak of iron oxides [30]. Fig. 4d shows that the N 1s spectrum has three separated peaks at 398.2, 400.5 and 401.2 eV, corresponding to pyridinic N (Pyri-N), pyrrolic N (Pyrr-N) and graphitic N (Grap-N), respectively [31].

2.2. Electrocatalytic activity toward ORR

To illustrate the tri-functional electrochemical performance of FeCNFs-NP, the ORR activity was firstly studied in alkaline solution. CV curves of FeCNFs-NP and Pt/C recorded in N_2 and O_2-saturated 0.1 M KOH are shown in Figure S3a and b. For FeCNFs-NP, an obvious reduction peak appears in O_2-saturated electrolyte but is absent in N_2-saturated electrolytes, and the peak centred at −0.098 V vs Ag/AgCl is 14 mV more positive than that of Pt/C, implying better ORR catalytic activity of FeCNFs-NP.

LSV curves of samples prepared under various conditions are displayed in Fig. 5a and Figure S3c. As depicted in Fig. 5a, FeCNFs-NP possesses the most positive onset potential (E_0, 0.017 V) and half wave potential ($E_{1/2}$, −0.083V), which are 35 mV and 45 mV more positive than that of Pt/C, respectively, demonstrating the excellent ORR activity of FeCNFs-NP. For Fesol-NP, its E_0 (−0.022 V) is comparable to that of Pt/C and slightly lower than that of FeCNF-NP, but its $E_{1/2}$ (−0.27 V) and limited current density are much worse compared to Pt/C and FeCNFs-NP. This is probably because its primary composition (Fe,N-doped carbon) is active for ORR, leading to a relatively positive E_0. However, the low surface area and irregular structure of Fesol-NP hinders the diffusion of reactant from electrolyte to the active sites inside catalyst, therefore resulting in an insufficient limited current [25]. This implies the significance of the microporous nanoparticles-embedded carbon nanofiber structure. To further probe the active species of ORR in FeCNFs-NP, the LSV curves of other control samples are studied and shown in Figure S3c. Briefly, the performance of FeCNFs-N is similar to that of FeCNFs-NP, indicating the phosphating process exerts few effects on the ORR activity. CNFs-N shows obvious ORR activity with E_0 of −0.145 V and limited current density of $-4\ mA\ cm^{-2}$, suggesting N-doped carbon is one of the active species for ORR. Such activity is resulted from the different electronegativity between N and C atom, which could create positively charged C atoms that are favorable for O_2 adsorption and subsequent reduction processes [24,32]. Though CNFs-N shows obvious ORR activity, its performance is much worse than that of FeCNFs-N (E_0 = 0.0153 V, $E_{1/2}$ = −0.08 V) which contains not only CNFs-N but also confined Fe_3O_4 nanocrystals. This implies the Fe_3O_4 nanocrystal, in this case, is another active species in ORR catalysis and the result is also consistent with previous work [6,14,33]. However, pure iron compounds, like iron oxides and nitrides, are normally less active for ORR due to low conductivity or surface area [34,35]. To prove this, the electrochemical impedance spectrum (EIS) measurements and corresponding equivalent circuits of FeCNFs-NP and pure Fe_3O_4 are also given in Figure S4 a and b, respectively. It is obvious that pure Fe_3O_4 shows larger semicircle than FeCNFs-NP, suggesting a higher charge-transfer resistance value of Fe_3O_4 [12]. Considering these phenomenon, it is reasonable to deduce that the dramatically promoted ORR activity of FeCNFs-NP could be resulted from the synergistic effect between Fe_3O_4 nanocrystals and N,P-doped CNFs shells [14,15]. Herein, the carbon shell could improve the overall conductivity, whereas iron species embedded in carbon

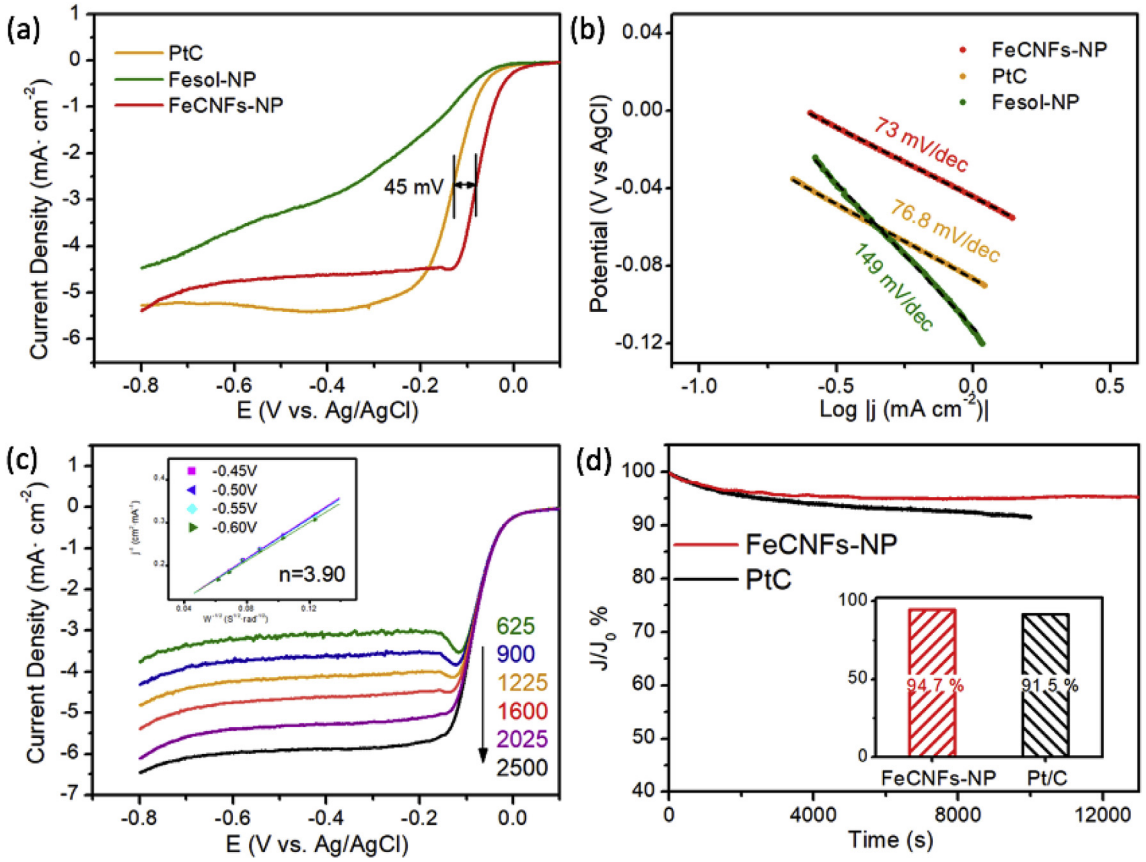

Fig. 5. (a) LSV curves of different samples in O_2-saturated 0.1 M KOH at 1600 rpm. (b) Tafel plots obtained from the RDE measurements in (a). (c) ORR polarization curves of FeCNFs-NP at various rotation rates in rpm. (The inset is the corresponding K–L plots at different potentials.) (d) Chronoamperometric (i–t) responses of FeCNFs-NP and Pt/C at −0.3 V in O_2-saturated 0.1 M KOH. (The inset is the retained ratio of the current density of FeCNFs-NP and Pt/C.)

layers can make surrounding carbon active for ORR, therefore further improving the ORR activity [36].

Further analysis on the catalytic kinetics of FeCNFs-NP, Pt/C and Fesol-NP by Tafel plots (Fig. 5b) shows that FeCNFs-NP has lower value of Tafel slope (η = 73 mv/dec) than those of Pt/C (η = 76.8 mV/dec) and Fesol-NP (η = 149 mV/dec), suggesting FeCNFs-NP possesses the faster electron transfer rate and more efficient reactant diffusion [37]. Likewise, the current density of FeCNFs-NP increases proportionally with the rate of rotations (Fig. 5c), yielding linearly fitted K–L plots (inset of Fig. 5c) which indicates the first-order reaction kinetics with respect to the concentration of dissolved oxygen. Based on slopes of K-L plots, the average electron transfer number (n_a) of FeCNFs-NP is calculated to be ~3.9 which nearly matches the theoretical value of Pt/C (4.0), implying FeCNFs-NP can catalyse the ORR via the $4e^-$ transfer path in alkaline solution.

In addition, FeCNFs-NP also exhibits superior stability (Fig. 5d) toward ORR in alkaline solutions. After 13000 s of continuous operation, 94.7% of current density remains due to the existence of carbon shell protecting Fe_3O_4 nanoparticles from losing in electrolyte. Whereas Pt/C shows a faster current loss, with 91.5% of current density retained only after 10000 s of continuous operation. The excellent ORR activity and stability, as well as low cost of FeCNFs-NP make it a potential substitution of current Pt/C catalysts.

2.3. Electrocatalytic activity toward HER and OER

The catalytic activities of as-made samples toward HER were performed in acid and basic solutions (Fig. 6 and Fig. S5). As shown in Fig. 6a and b, commercial Pt/C owns the best HER activity in acid solutions with the lowest overpotential at the current density of 10 mA cm^{-2} (η_{10}). Among the as-prepared samples, FeCNFs-NP exhibits the best performance, with the value of η_{10} to be 149 mV, much lower than that of FeCNFs-N (η_{10} = 240 mV), suggesting FeP generated during the phosphating process remarkably promotes the HER catalytic activity and therefore being the main HER active species. Herein, phosphorus in FeP could act as the proton-acceptor to initiate the HER and weaken the bond strength between metal and adsorbed hydrogen [38,39]. Moreover, turnover frequencies (TOFs) of FeCNFs-NP and FeCNFs-N at the overpotential of 200 mV were also calculated. The detailed calculation process is shown in supplementary information. The TOF of FeCNFs-NP is 0.072 s^{-1}, which is almost tenfold higher than that of FeCNFs-N (TOF = 0.0079 s^{-1}), implying the much better HER performance for FeCNFs-NP. Besides, CNFs-NP shows a very high value of η_{10}, indicating the pure N,P-doped carbon has low HER activity. After comparing the performance of FeCNFs-N and CNFs-NP, it can be deduced that iron oxides are also beneficial to the HER catalysis by providing the water dissociation sites for HER [9,40]. According to previous modeling calculation, adding FeO_x clusters on FeP (011) surfaces leads to increased adsorption energy for water molecule which means enhanced water affinity [40]. GCE is inactive toward HER, which proves the activities of other samples are truly reflected. Fig. 6c shows that the slope of the Tafel plot for the Pt/C is 29 mV/dec, which is consistent with that expected for the known HER mechanism on Pt [41]. FeCNFs-NP has Tafel slope of 58 mv/dec, much lower than that of FeCNFs-N, further proving the outstanding HER activity of FeCNFs-NP. Besides, FeCNFs-NP also possesses robust stability in acid solutions, with LSV curve only showing slightly negative shift after 1000 continuous CV cycles (Fig. 6d). The high stability can be ascribed to the nanoparticles-embedded nanofiber structure which protects the iron compounds inside CNFs from fast etching by acid solutions [23]. The

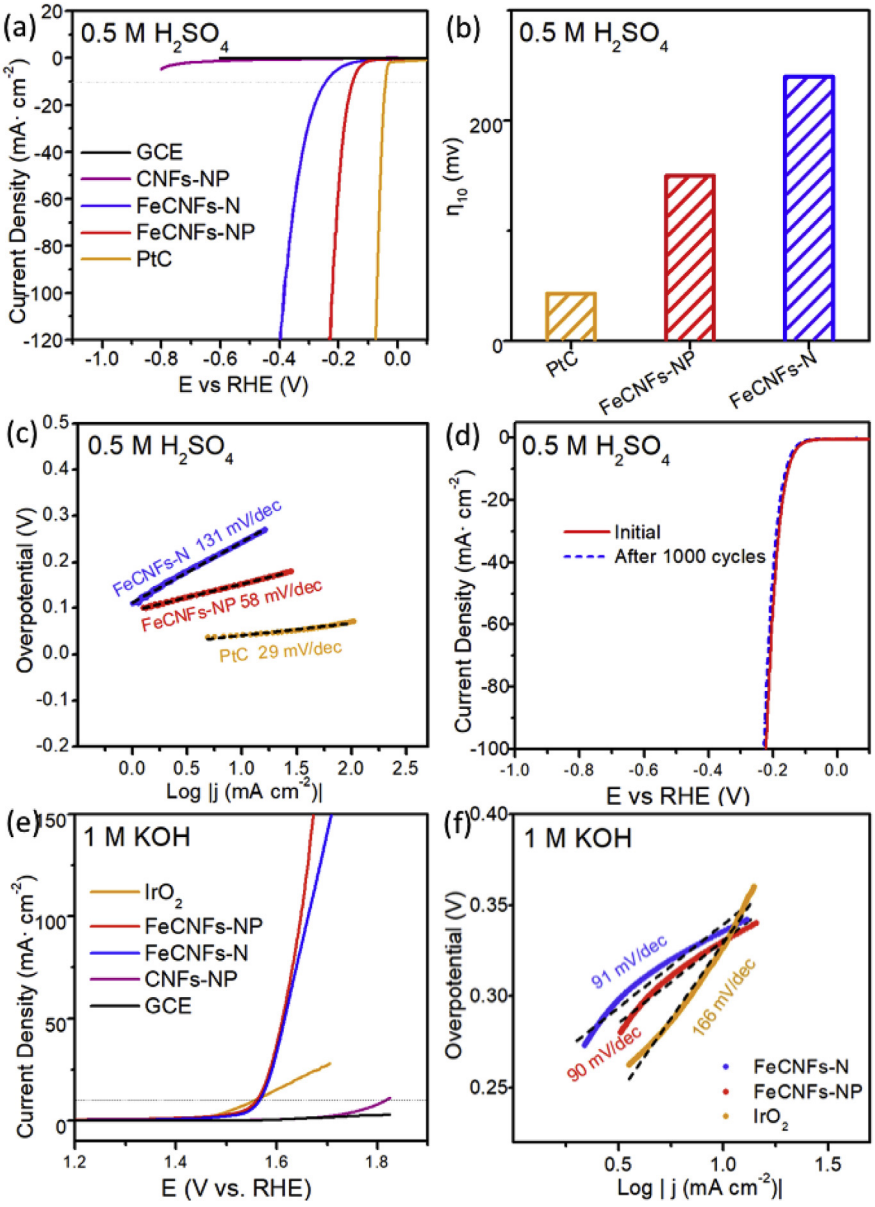

Fig. 6. (a) Comparative HER polarization curves in 0.5 M H_2SO_4 with a scan rate of 2 mV s^{-1}, (b) Corresponding η_{10} and (c) Corresponding HER Tafel plots. (d) Initial and 1000th cycle HER polarization curves of FeCNFs-NP in 0.5 M H_2SO_4. (e) Comparative OER polarization curves in 1 M KOH and (f) Corresponding OER Tafel plots.

HER activities of such samples in alkaline solutions were also tested (Figure S5a and b), and they show the same trend as that in acid solutions. The performance order is FeCNFs-NP > FeCNF-N > CNFs-NP. Although the HER performances of FeCNFs-NP in acid and basic solutions are inferior to commercial Pt/C, they are still comparable to or better than other previously reported bifunctional or tri-functional catalysts [42–46]. To the best of our knowledge, there is still no report on tri-functional catalysts whose HER performance is better than Pt/C.

In addition to HER performance, FeCNFs-NP also exhibits impressive OER activity. As depicted in Fig. 6e, FeCNFs-NP has the onset potential of 1.56 V vs RHE which is 10 mV higher than that of commercial IrO_2, suggesting the excellent OER activity of FeCNFs-NP. FeCNFs-N shows a similar onset potential to FeCNFs-NP, but a lower current density when the potential is over 1.62 V vs RHE, implying that FeP is beneficial for the catalysis of OER at higher potential. CNFs-NP displays certain OER activity compared to bare GCE, however, its onset potential (> 1.8 V vs RHE) is much higher than those of FeCNFs-N and FeCNFs-NP, both of which mainly containing Fe_3O_4 nanocrystals. Therefore, it is reasonable to conclude that both Fe_3O_4 and N,P-doped carbon are active species for OER and promote the OER activity, which also have been verified by many other studies [5,47–49]. Specifically, carbon atoms bonding with N will be positively charged and adsorb the OH^- and accelerate the electron transfer between catalyst surfaces and reaction intermediates, therefore increasing the OER activity [48]. Whereas, Fe_3O_4 with a reverse spinel crystal structure is good for electron transportation between Fe^{3+} and Fe^{2+} ions [34], and can directly provide lattice oxygen as one of the sources of generated O_2 during OER, thus promoting OER catalysis [49]. The tafel slope of FeCNFs-NP (90 mV/dec) is the lowest among all samples (Fig. 6f), suggesting a quicker kinetic process of FeCNFs-NP compared to IrO_2 and other control samples. The OER stability of FeCNFs-NP was also tested and shown in Figure S5c. The onset potential of FeCNFs-NP displays a positive shift after 500 continuous CV cycles, which probably due to the oxidation of carbon support [50]. Finally, the CV curve of FeCNFs-NP scanned in whole potential range from HER to OER (Fig. S6) once again proves the good catalytic activity of FeCNFs-NP as advanced

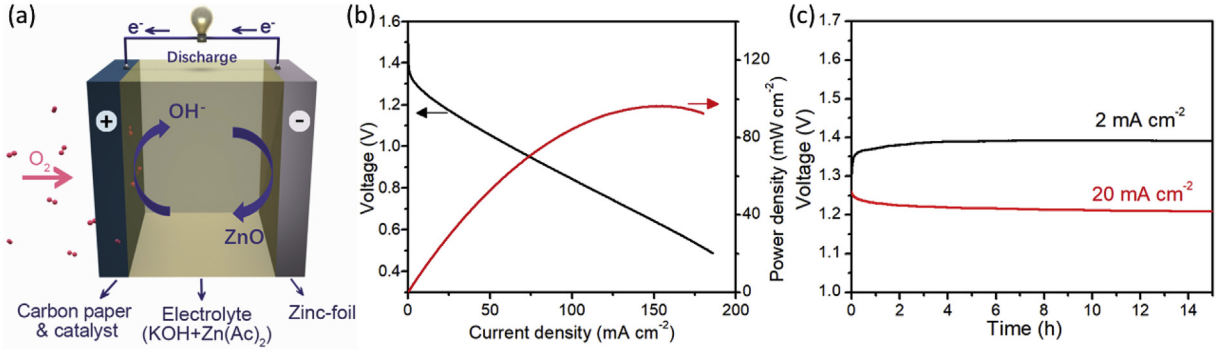

Fig. 7. (a) Schematic illustration of the two-electrode disposable zinc–air battery. (b) Polarization curve (V-i) and corresponding power density plots. (c) long-time discharge curve of the zinc-air battery with FeCNFs-NP as the electrode catalyst.

tri-functional catalyst.

2.4. Application in zinc-air batteries

In addition, the potential application of FeCNFs-NP catalyst in disposable zinc-air batteries was also investigated (Fig. 7). A home-made two-electrode disposable zinc–air battery was fabricated according to Fig. 7a. In this battery, when the cathode is exposed to air, O_2 can reach cathode and is reduced to OH^- (ORR process) by the catalyst. Then the formed OH^- ions travel to anode (Zn foil) and combine with Zn to form $Zn(OH)_4^{2-}$. Subsequently, the electrons are released to produce the voltage. The $Zn(OH)_4^{2-}$ finally decomposes into ZnO and water which goes back to electrolyte. Fig. 7b shows the discharge polarization curve of the battery with an open circuit voltage as high as ≈ 1.4 V. The maximum power density of zinc-air battery with FeCNFs-NP electrode is 97 mW cm^{-2}, which is comparable to many other catalysts [4,51]. Besides, the zinc-air battery made with FeCNFs-NP is also very stable. When galvanostatically discharged at 2 mA cm^{-2} or 20 mA cm^{-2}, no obvious voltage drop is observed (Fig. 7c) owing to the stable structure of FeCNFs-NP [52].

3. Conclusions

In conclusion, Fe_3O_4 and FeP nanoparticles embedded in N,P-doped carbon nanofibers were successfully synthesized via electrospinning, carbonization and phosphating processes. This novel catalyst exhibited excellent tri-functional catalytic activity toward ORR, HER and OER. Herein, the microporous nanoparticles-embedded nanofiber structure provided easy and fast mass transport pathways and protection against the electrolyte erosion, therefore promoting the ORR activity as well as stabilities. Fe_3O_4 and N,P-doped carbon were found to play important roles in catalysis of ORR and OER, and beneficial to HER catalysis, while FeP, as the main HER active species in catalysts, remarkably boosted the HER activity. Besides, the synergistic effect exists between N,P-doped carbon shells and encapsulated Fe_3O_4/FeP nanocrystals, leading to much better electrochemical performance of FeCNFs-NP than that of bare N,P-doped carbon shells. Interestingly, the catalyst also showed robust performance when used in disposable zin-air batteries. Our work provides an effective method to synthesize the tri-functional electrochemical catalyst which is promising to be widely applied in electrochemical conversion devices.

4. Material and methods

4.1. Chemicals

Polyacrylonitrile (PAN, Mw = 150,000 g mol^{-1}), N,N-dimethylformamide (DMF, ≥ 99.5%), iron(III) acetylacetonate (Fe$(acac)_3$, 98%) were purchased from Macklin Reagent (Shanghai, China). Urea, NaH_2PO_2, H_2SO_4, KOH were purchased from Shanghai Lingfeng Chemical Reagent Co., LTD (China). The deionized water (DI water, R = 18.2 MΩ) used in all experiments was purified through a Millipore system.

4.2. Synthetic procedures

First, Fe/PAN NFs were fabricated by electrospinning. Specifically, PAN was dissolved in 10 mL DMF at room temperature with the concentration of 8%. Then 1 g Fe$(acac)_3$ was added into PAN solution, and the mixture was stirred at room temperature for 12 h to attain homogeneous precursor solution. This solution was loaded into a plastic syringe with a stainless-steel needle connected to high voltage of 12 kV. A piece of aluminum foil was placed 15 cm in front of the needle to collect the Fe/PAN NFs. Second, the Fe/PAN NFs were stabilized in quartz tube furnace under air atmosphere at 240 °C for 6 h with a heating rate (HR) of 5 °C/min. In this process, thermoplastic PAN was converted to a non-plastic cyclic or ladder compound [53], with the colour of nanofibers turned from orange to brown. The obtained product is marked as FePAN-O. Third, for preparing the FeCNFs-N, 150 mg FePAN-O and 3 g urea were put into separate porcelain boats with urea at upstream side of the furnace and heated at 800 °C (HR 5 °C/min) for 2 h under N_2 atmosphere, after that its colour turned to black. Finally, the phosphating process was conducted by annealing FeCNFs-N and NaH_2PO_2 at 350 °C (HR 5 °C/min) for 1 h under N_2 atmosphere, with NaH_2PO_2 in another porcelain boats at the upstream side of furnace. The weight ratio for FeCNFs-N and NaH_2PO_2 is 1:3. The final product was denoted by FeCNFs-NP. To study the mechanism of activity of catalysts, control samples are also prepared. CNFs-N and CNFs-NP were made under the same conditions as FeCNFs-N and FeCNFs-NP, respectively, only without adding iron salts. Fesol-NP was synthesized by directly evaporating the solvent of precursor solution under 50 °C without using electrospinning method, but with the same experimental conditions as FeCNFs-NP.

Funding sources

National Natural Science Foundation of China (No. 51672204) and National Key Research and Development Program of China (No. 2016YFA0202603).

Acknowledgment

We thank Dr. Yushi Yang for his help with graphics, Rietveld refinement and constructive discussions. This work is financially supported by the National Key Research and Development Program of China (No. 2016YFA0202603) and the National Natural Science Foundation of China (Grant No. 51672204).

Appendix A. Supplementary data

Supplementary data to this article can be found online at https://doi.org/10.1016/j.jpowsour.2018.12.056.

References

[1] L. Han, S. Dong, E. Wang, Transition-metal (Co, Ni, and Fe)-Based electrocatalysts for the water oxidation reaction, Adv. Mater. 28 (2016) 9266–9291, https://doi.org/10.1002/adma.201602270.

[2] M. Shao, Q. Chang, J.-P. Dodelet, R. Chenitz, Recent advances in electrocatalysts for oxygen reduction reaction, Chem. Rev. 116 (2016) 3594–3657, https://doi.org/10.1021/acs.chemrev.5b00462.

[3] P. Du, R. Eisenberg, Catalysts made of earth-abundant elements (Co, Ni, Fe) for water splitting: recent progress and future challenges, Energy Environ. Sci. 5 (2012) 6012, https://doi.org/10.1039/c2ee03250c.

[4] P. Chen, T. Zhou, L. Xing, K. Xu, Y. Tong, H. Xie, et al., Atomically dispersed iron–nitrogen species as electrocatalysts for bifunctional oxygen evolution and reduction reactions zuschriften, Angew. Chem. 128 (2016) 1–6, https://doi.org/10.1002/ange.201610119.

[5] J. Yang, G. Zhu, Y. Liu, J. Xia, Z. Ji, X. Shen, et al., Fe_3O_4-Decorated Co_9S_8 nanoparticles in situ grown on reduced graphene oxide: a new and efficient electrocatalyst for oxygen evolution reaction, Adv. Funct. Mater. 26 (2016) 4712–4721, https://doi.org/10.1002/adfm.201600674.

[6] Z. Wu, S. Yang, Y. Sun, K. Parvez, X. Feng, K. Müllen, 3D nitrogen-doped graphene aerogel-supported Fe_3O_4 nanoparticles as efficient electrocatalysts for the oxygen reduction reaction, J. Am. Chem. Soc. 134 (2012) 9082–9085, https://doi.org/10.1021/ja3030565.

[7] F. Yu, H. Zhou, Z. Zhu, J. Sun, R. He, J. Bao, et al., Three-dimensional nanoporous iron nitride film as an efficient electrocatalyst for water oxidation, ACS Catal. 7 (2017) 2052–2057, https://doi.org/10.1021/acscatal.6b03132.

[8] J.X. Feng, H. Xu, Y.T. Dong, S.H. Ye, Y.X. Tong, G.R. Li, FeOOH/Co/FeOOH hybrid nanotube Arrays as high-performance electrocatalysts for the oxygen evolution reaction, Angew. Chem. Int. Ed. 55 (2016) 3694–3698, https://doi.org/10.1002/anie.201511447.

[9] R. Subbaraman, D. Tripkovic, K.-C. Chang, D. Strmcnik, A.P. Paulikas, P. Hirunsit, et al., Trends in activity for the water electrolyser reactions on 3d M(Ni,Co,Fe,Mn) hydr(oxy)oxide catalysts, Nat. Mater. 11 (2012) 550–557, https://doi.org/10.1038/nmat3313.

[10] C. Lv, Z. Peng, Y. Zhao, Z. Huang, C. Zhang, The hierarchical nanowires array of iron phosphide integrated on a carbon fiber paper as an effective electrocatalyst for hydrogen generation, J. Mater. Chem. A. 4 (2016) 1454–1460, https://doi.org/10.1039/C5TA08715E.

[11] P. Jiang, Q. Liu, Y. Liang, J. Tian, A.M. Asiri, X. Sun, A cost-effective 3D hydrogen evolution cathode with high catalytic activity: FeP nanowire array as the active phase, Angew. Chem. Int. Ed. 53 (2014) 12855–12859, https://doi.org/10.1002/anie.201406848.

[12] Y. Li, H. Zhang, M. Jiang, Q. Zhang, P. He, X. Sun, 3D self-supported Fe-doped Ni_2P nanosheet arrays as bifunctional catalysts for overall water splitting, Adv. Funct. Mater. 27 (2017) 1–8, https://doi.org/10.1002/adfm.201702513.

[13] G. Ren, X. Lu, Y. Li, Y. Zhu, L. Dai, L. Jiang, Porous core-shell Fe_3C embedded N-doped carbon nanofibers as an effective electrocatalysts for oxygen reduction reaction, ACS Appl. Mater. Interfaces 8 (2016) 4118–4125, https://doi.org/10.1021/acsami.5b11786.

[14] H. Wang, W. Wang, M. Gui, M. Asif, Z. Wang, Y. Yu, et al., Uniform Fe_3O_4/nitrogen-doped mesoporous carbon spheres derived from ferric citrate-bonded melamine resin as an efficient synergistic catalyst for oxygen reduction, ACS Appl. Mater. Interfaces 9 (2017) 335–344, https://doi.org/10.1021/acsami.6b11608.

[15] Y.Y. Liang, Y.G. Li, H.L. Wang, J.G. Zhou, J. Wang, T. Regier, et al., Co_3O_4 nanocrystals on graphene as a synergistic catalyst for oxygen reduction reaction, Nat. Mater. 10 (2011) 780–786.

[16] D. Ji, S. Peng, J. Lu, L. Li, S. Yang, G. Yang, et al., Design and synthesis of porous channel-rich carbon nanofibers for self-standing oxygen reduction reaction and hydrogen evolution reaction bifunctional catalysts in alkaline medium, J. Mater. Chem. A. 5 (2017) 7507–7515, https://doi.org/10.1039/C7TA00828G.

[17] X. Wang, Y. Li, T. Jin, J. Meng, L. Jiao, M. Zhu, et al., Electrospun thin-walled $CuCo_2O_4$@C nanotubes as bifunctional oxygen electrocatalysts for rechargeable Zn-air batteries, Nano Lett. 17 (2017) 7989–7994, https://doi.org/10.1021/acs.nanolett.7b04502.

[18] J. Guo, Q. Niu, Y. Yuan, I. Maitlo, J. Nie, G. Ma, Electrospun core-shell nanofibers derived Fe-S/N doped carbon material for oxygen reduction reaction, Appl. Surf. Sci. 416 (2017) 118–123, https://doi.org/10.1016/j.apsusc.2017.04.135.

[19] L.-F. Chen, Y. Lu, L. YU, X.W.D. Lou, Designed formation of hollow particle-based nitrogen-doped carbon nanofibers for high-performance supercapacitors, Energy Environ. Sci. 8 (2017), https://doi.org/10.1039/C7EE00488E.

[20] Z.Q. Liu, H. Cheng, N. Li, T.Y. Ma, Y.Z. Su, $ZnCo_2O_4$ quantum dots anchored on nitrogen-doped carbon nanotubes as reversible oxygen reduction/evolution electrocatalysts, Adv. Mater. 28 (2016) 3777–3784, https://doi.org/10.1002/adma.201506197.

[21] H. Li, P. Wen, Q. Li, C. Dun, J. Xing, C. Lu, et al., Earth-abundant iron diboride (FeB_2) nanoparticles as highly active bifunctional electrocatalysts for overall water splitting, Adv. Energy Mater. 7 (2017) 1–12, https://doi.org/10.1002/aenm.201700513.

[22] S.K. Nataraj, K.S. Yang, T.M. Aminabhavi, Polyacrylonitrile-based nanofibers - a state-of-the-art review, Prog. Polym. Sci. 37 (2012) 487–513, https://doi.org/10.1016/j.progpolymsci.2011.07.001.

[23] D.Y. Chung, S.W. Jun, G. Yoon, H. Kim, J.M. Yoo, K.S. Lee, et al., Large-scale synthesis of carbon-shell-coated FeP nanoparticles for robust hydrogen evolution reaction electrocatalyst, J. Am. Chem. Soc. 139 (2017) 6669–6674, https://doi.org/10.1021/jacs.7b01530.

[24] Q. Liu, Y. Wang, L. Dai, J. Yao, Scalable fabrication of nanoporous carbon fiber films as bifunctional catalytic electrodes for flexible Zn-air batteries, Adv. Mater. 28 (2016) 3000–3006, https://doi.org/10.1002/adma.201506112.

[25] H.W. Liang, W. Wei, Z.S. Wu, X.L. Feng, K. Müllen, Mesoporous metal − nitrogen-doped carbon electrocatalysts for highly efficient oxygen reduction reaction, J. Am. Chem. Soc. 135 (2013) 16002–16005, https://doi.org/10.1021/ja407552k.

[26] Z. Pu, S. Wei, Z. Chen, S. Mu, Flexible molybdenum phosphide nanosheet array electrodes for hydrogen evolution reaction in a wide pH range, Appl. Catal. B Environ. 196 (2016) 193–198, https://doi.org/10.1016/j.apcatb.2016.05.027.

[27] P. Wang, Z. Pu, Y. Li, L. Wu, Z. Tu, M. Jiang, et al., Iron-doped nickel phosphide nanosheet arrays: an efficient bifunctional electrocatalyst for water splitting, ACS Appl. Mater. Interfaces 9 (2017) 26001–26007, https://doi.org/10.1021/acsami.7b06305.

[28] Y. Yan, B.Y. Xia, X. Ge, Z. Liu, A. Fisher, X. Wang, A flexible electrode based on iron phosphide nanotubes for overall water splitting, Chem. Eur J. 21 (2015) 18062–18067, https://doi.org/10.1002/chem.201503777.

[29] C.E. Myers, H.F. Franzen, J.W. Anderegg, X-ray photoelectron spectra and bonding in transition-metal phosphides, Inorg. Chem. 24 (1985) 1822–1824, https://doi.org/10.1021/ic00206a025.

[30] T. Yamashita, P. Hayes, Analysis of XPS spectra of Fe^{2+} and Fe^{3+} ions in oxide materials, Appl. Surf. Sci. 254 (2008) 2441–2449, https://doi.org/10.1016/j.apsusc.2007.09.063.

[31] K. Parvez, S. Bin Yang, Y. Hernandez, A. Winter, A. Turchanin, X.L. Feng, et al., Nitrogen-doped graphene and its iron-based composite as efficient electrocatalysts for oxygen reduction reaction, ACS Nano 6 (2012) 9541–9550, https://doi.org/10.1021/nn302674k.

[32] K.P. Gong, F. Du, Z.H. Xia, M. Durstock, L.M. Dai, Nitrogen-doped carbon nanotube arrays with high electrocatalytic activity for oxygen reduction, Science 323 (2009) 760–764.

[33] S. Gao, B. Fan, R. Feng, C. Ye, X. Wei, J. Liu, et al., N-doped-carbon-coated Fe_3O_4 from metal-organic framework as efficient electrocatalyst for ORR, Nanomater. Energy 40 (2017) 462–470, https://doi.org/10.1016/j.nanoen.2017.08.044.

[34] L. Xu, Q. Jiang, Z. Xiao, X. Li, J. Huo, S. Wang, et al., Plasma-engraved Co_3O_4 nanosheets with oxygen vacancies and high surface area for the oxygen evolution reaction, Angew. Chem. Int. Ed. 55 (2016) 5277–5281, https://doi.org/10.1002/anie.201600687.

[35] M. Wang, Y. Yang, X. Liu, Z. Pu, Z. Kou, P. Zhu, et al., The role of iron nitrides in the Fe–N–C catalysis system towards the oxygen reduction reaction, Nanoscale 9 (2017) 7641–7649, https://doi.org/10.1039/C7NR01925D.

[36] J. Wei, Y. Liang, Y. Hu, B. Kong, G.P. Simon, J. Zhang, et al., A versatile iron-tannin-framework ink coating strategy to fabricate biomass-derived iron carbide/Fe-N-carbon catalysts for efficient oxygen reduction, Angew. Chem. Int. Ed. 55 (2016) 1355–1359, https://doi.org/10.1002/anie.201509024.

[37] Z.H. Li, M.F. Shao, L. Zhou, R.K. Zhang, C. Zhang, M. Wei, et al., Directed growth of metal-organic frameworks and their derived carbon-based network for efficient electrocatalytic oxygen reduction, Adv. Mater. 28 (2016) 2337–2344, https://doi.org/10.1002/adma.201505086.

[38] P. Xiao, W. Chen, X. Wang, A review of phosphide-based materials for electrocatalytic hydrogen evolution, Adv. Energy Mater. 5 (2015) 1–13, https://doi.org/10.1002/aenm.201500985.

[39] G.F. Chen, T.Y. Ma, Z.Q. Liu, N. Li, Y.Z. Su, K. Davey, et al., Efficient and stable bifunctional electrocatalysts Ni/Ni_xM_y (M = P, S) for overall water splitting, Adv. Funct. Mater. 26 (2016) 3314–3323, https://doi.org/10.1002/adfm.201505626.

[40] J. Huang, Y. Su, Y. Zhang, W. Wu, C. Wu, FeO_x/FeP hybrid nanorods neutral hydrogen evolution electrocatalysis : insight into interface, J. Mater. Chem. A Mater. Energy Sustain. 6 (2018) 9467–9472, https://doi.org/10.1039/C8TA02204F.

[41] E.J. Popczun, C.G. Read, C.W. Roske, N.S. Lewis, R.E. Schaak, Highly active electrocatalysis of the hydrogen evolution reaction by cobalt phosphide nanoparticles, Angew. Chem. Int. Ed. 53 (2014) 5427–5430, https://doi.org/10.1002/anie.201402646.

[42] J. Yang, X. Wang, B. Li, L. Ma, L. Shi, Y. Xiong, et al., Novel iron/cobalt-containing polypyrrole hydrogel-derived trifunctional electrocatalyst for self-powered overall water splitting, Adv. Funct. Mater. 27 (2017) 1606497, https://doi.org/10.1002/adfm.201606497.

[43] I.S. Amiinu, Z. Pu, X. Liu, K.A. Owusu, H. Gabriela, R. Monestel, et al., Multifunctional Mo – N/C @ MoS_2 electrocatalysts for HER , OER , ORR , and Zn – air batteries, Adv. Funct. Mater. 27 (2017) 1702300, , https://doi.org/10.1002/adfm.201702300.

[44] M. Jahan, Z. Liu, K.P. Loh, A graphene oxide and copper-centered metal organic framework composite as a tri-functional catalyst for HER, OER, and ORR, Adv. Funct. Mater. 23 (2013) 5363–5372, https://doi.org/10.1002/adfm.201300510.

[45] C. Tang, L. Zhong, B. Zhang, H.F. Wang, Q. Zhang, 3D mesoporous van der Waals heterostructures for trifunctional energy electrocatalysis, Adv. Mater. 30 (2018) 1–8, https://doi.org/10.1002/adma.201705110.

[46] A.H. Zhang, Q. Yun, Q. Lu, X. Zhang, Bimetallic Zn/Fe polyphthalocyanine derived single-atom Fe-N_4 catalytic site:A superior tri-functional catalyst for overall water splitting and Zn-air battery, Angew. Chem. (2018), https://doi.org/10.1002/ange.201706426.

[47] Y. Zhao, R. Nakamura, K. Kamiya, S. Nakanishi, K. Hashimoto, Nitrogen-doped carbon nanomaterials as non-metal electrocatalysts for water oxidation, Nat.

Commun. 4 (2013) 1–7, https://doi.org/10.1038/ncomms3390.
[48] S. Chen, J. Duan, M. Jaroniec, S.Z. Qiao, Nitrogen and oxygen dual-doped carbon hydrogel film as a substrate-free electrode for highly efficient oxygen evolution reaction, Adv. Mater. 26 (2014) 2925–2930, https://doi.org/10.1002/adma.201305608.
[49] Y. Zhang, T.R. Chang, B. Zhou, Y.T. Cui, H. Yan, Z. Liu, et al., Direct observation of the transition from indirect to direct bandgap in atomically thin epitaxial $MoSe_2$, Nat. Nanotechnol. 9 (2014) 111–115, https://doi.org/10.1038/nnano.2013.277.
[50] W. Wang, J. Luo, S. Chen, Carbon oxidation reactions could misguide the evaluation of carbon black-based oxygen-evolution electrocatalysts, Chem. Commun. 53 (2017) 11556–11559, https://doi.org/10.1039/C7CC04611A.
[51] J. Zhu, H. Zhou, C. Zhang, J. Zhang, S. Mu, Dual active nitrogen doped hierarchical porous hollow carbon nanospheres as an oxygen reduction electrocatalyst for zinc–air batteries, Nanoscale 9 (2017) 13257–13263, https://doi.org/10.1039/C7NR04349J.
[52] Y. Li, M. Gong, Y. Liang, J. Feng, J.E. Kim, H. Wang, et al., Advanced zinc-air batteries based on high-performance hybrid electrocatalysts, Nat. Commun. 4 (2013) 1805–1807, https://doi.org/10.1038/ncomms2812.
[53] H. Hou, D.H. Reneker, Carbon nanotubes on carbon nanofibers: a novel structure based on electrospun polymer nanofibers, Adv. Mater. 16 (2004) 69–73, https://doi.org/10.1002/adma.200306205.